Tribology International 175 (2022) 107793

Contents lists available at ScienceDirect

Tribology International

journal homepage: www.elsevier.com/locate/triboint

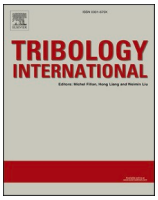

Interfacial slip verification and slip defect identification in shrink-fitted bimetallic sleeve roll used in hot rolling mill

Nao-Aki Noda *, Rahimah Abdul Rafar, Yudai Taruya, Xuchen Zheng, Hiroyuki Tsurumaru, Yoshikazu Sano, Yasushi Takase, Ko Nakagawa, Keisuke Kondo

Mechanical Engineering Department, Kyushu Institute of Technology, 1–1 Sensui-cho, Tobata-ku, Kitakyushu-shi 804-8550, Japan

ARTICLE INFO

Keywords:
Rolling roll
Shrink-fitted
Interfacial slip
Bimetallic roll
Sleeve
Shaft

ABSTRACT

Shrink-fitted sleeve rolls have several advantages including the ability to reuse shafts by replacing worn sleeves and the ability to apply to next-generation rolls. However, the authors' previous simulation showed a "non-uniform slip" may appear between the shaft and the shrink-fitted sleeve even under free rolling and when no overall uniform slip condition is satisfied. In this paper, the rolling experiment is conducted by using a miniature rolling mill to verify the slip phenomenon realized by the numerical simulation. To understand the phenomenon, the slip defect formation and the slip growth are investigated by observing the slipped surfaces in detail. It is found that the slip defect starts from the contact of the surface roughness where the width of the defect coincides with the pitch of the machining feed. Eventually, the slip defect is developed by erosion wear and cohesive wear during the rolling and finally forming a large oval-shaped erosion groove at the end of the scratch. Finally, the fatigue strength of the sleeve roll is evaluated by considering the slip defect geometry observed from the experiment.

1. Introduction

In steel manufacturing industries, rolling process produces more tonnage than any other metalworking processes [1–24]. Among the rolls used in steel rolling, sleeve assembly type rolls were developed by shrink-fitting the shaft to the sleeve instead of solid rolls. Some of the sleeve rolls are successfully and practically used as back-up rolls with a large body diameter exceeding 1000 mm and large H-shaped steel rolling rolls [1–3]. Sleeve assembly rolls have several advantages including the ability to reuse shafts by replacing worn sleeves and the ability to apply to next-generation rolls. Nowadays, work rolls are still being developed with an emphasis placed on better wear resistance and structural toughness [4]. For the practical development of super cermet rolls and ceramic rolls [5,6], the sleeve assembly type structure is essential. To meet these requirements, a new composite roll and a bimetallic sleeve roll were also developed by applying a shrink-fitted structure [7].

However, this shrink-fitted sleeve roll has several peculiar problems such as residual bend deformation, fretting fatigue cracks at the sleeve end and sleeve fracture due to the circumferential sleeve slip [5–11]. In particular, it is known that even though the frictional resistance torque of the shrink fit part is larger than the motor torque, the sleeve slips in the circumferential direction severely [10–13]. A similar slip is known in ball/roller bearing named "an interface creep", where the slip occurs even under free rolling between the shaft and the inner race as well as between the housing and the outer race [25–37]. Since few studies treated such slips quantitatively, the authors performed a numerical simulation to realize the interfacial slip under free rolling while considering the work roll of 4-high rolling mill (see Fig. 1a) [20]. The results showed that an interfacial slip can be expressed as an accumulation of non-uniform slips. After confirming the slip under free rolling, the authors clarified that the slip is accelerated largely by the motor torque [21] considering several design factors such as the elastic shaft deformation, shrink-fitting ratio and friction coefficient [22,23]. The results showed that the slip acceleration is explained from the slip region and the low stress region [20–23]. However, detailed experimental validation of the simulation has not yet been shown.

Fig. 1 illustrates a miniature rolling mill whose dimension is approximately 1/10 from the real rolling mill. In this study, by using the miniature rolling mill, a rolling experiment is conducted to confirm the circumferential slip experimentally. To verify the numerical simulation, the miniature roll in Fig. 1 will be analyzed to be compared to the experiment. Since a similar phenomenon is known as an interface creep

* Corresponding author.
E-mail address: noda.naoaki844@mail.kyutech.jp (N.-A. Noda).

https://doi.org/10.1016/j.triboint.2022.107793
Received 10 May 2022; Received in revised form 29 June 2022; Accepted 16 July 2022
Available online 20 July 2022

Nomenclature

A	point in Fig.17 considering $\left(\sigma_\theta^{Res+Shrink}+\sigma_\theta^{Rolling}\right)\times K_t$ (MPa).
A'	point in Fig.17 considering $\left(\sigma_\theta^{Res+Shrink}+\sigma_\theta^{Rolling}\right)\times K_t$ (MPa).
D	outer diameter of the sleeve (mm).
D_B	body diameter of roll (mm).
DCI	ductile casting iron.
d	inner diameter of sleeve Fig. 3b (mm).
d_1	outer diameter of shaft Fig. 3b (mm).
E	Young's modulus of sleeve (GPa).
E_s	Young's modulus of shaft (GPa)
FEM	finite element method.
HB	hardness Brinell.
HSS	high-speed steel.
H_v	vickers hardness (kgf/mm^2).
K_t	stress concentration factor.
n	number of rotations.
$n_t - n_0$	total number of rotations of the roll.
P	load from back-up roll (Experimental condition) (ton).
P	concentrated load per unit width (Analytical condition) (N/mm).
P_0	concentrated load per unit width = Standard compressive force (N/mm).
P_b	bending force from bearing per unit width (Nm/mm).
S	frictional force from the rolling plate per unit width (N/mm).
T	driving torque (Nm).
T_m	motor torque per unit width = Standard driving torque (Nm/mm).
T_r	slippage resistance torque (Nm/mm).
$u_\theta(\theta)$	interfacial displacement (mm).
u_θ^{sleeve}	circumferential displacement of the sleeve (mm).
u_θ^{shaft}	circumferential displacement of the shaft (mm).
$u_\theta^{P(0)\sim P(\varphi)}(\theta)$	interfacial slip u_θ when the pair of loads $P = P_0$ are applied at $\varphi = 0$ ($\varphi = \pi$) to $\varphi = \varphi$ ($\varphi = \varphi + \pi$) defined in Fig. 4 (mm).
$u_{\theta,ave.}^{P(0)\sim P(\varphi)}$	average displacement due to the pair of loads shifting from $\varphi = 0$ ($\varphi = \pi$) to $\varphi = \varphi$ ($\varphi = \varphi + \pi$) (mm).
$u_{\theta,T=T_m}^{P(0)\sim P(\varphi)}(\theta)$	interfacial slip u_θ under standard drive torque $T = T_m$ when the pair of loads $P = P_0$ are applied at $\varphi = 0$ ($\varphi = \pi$) to $\varphi = \varphi$ ($\varphi = \varphi + \pi$) (mm).
$u_{\theta,ave.T=T_m}^{P(0)\sim P(\varphi)}$	average displacement under standard drive torque $T = T_m$ due to the pair of loads $P = P_0$ shifting from $\varphi = 0$ ($\varphi = \pi$) to $\varphi = \varphi$ ($\varphi = \varphi + \pi$) (mm).
ξ	effective shrink-fitting ratio considering manufacturing error.
δ	tightening allowance between sleeve inner diameter and shaft outer diameter (mm).
δ/d	shrink-fitting ratio.
θ	circumferential displacement angle (°).
θ_{slip}	slip angle (°).
μ	friction coefficient between sleeve and shaft.
υ	Poisson's ratio of steel sleeve.
υ_s	Poisson's ratio of shaft.
σ_a	stress amplitude (MPa).
σ_B	ultimate tensile strength (MPa).
σ_m	mean stress (MPa).
$\sigma_{r_{shrink}}$	shrink-fitting stress (MPa).
σ_θ	rolling stress at the inner surface of the sleeve (MPa).
$\sigma_{\theta max}$	maximum stress (MPa).
$\sigma_{\theta min}$	minimum stress (MPa).
$\sigma_{\theta,shrink}$	interface stress during shrink-fitting (MPa).
$\sigma_{\theta max}^{P_0}$	maximum stress under the load $P = P_0$ (MPa).
$\sigma_{\theta min}^{P_0}$	minimum stress under the load $P = P_0$ (MPa).
$\sigma_{\theta max}^{1.5P_0}$	maximum stress under the load $P = 1.5P_0$ (MPa).
$\sigma_{\theta min}^{1.5P_0}$	minimum stress under the load $P = 1.5P_0$ (MPa).
$\sigma_{\theta,T=T_m}^{P(0)\sim P(4\pi)}(\theta)$	interface stress σ_θ under standard drive torque $T = T_m$ due to the load $P = P_0$ moves two rotations (MPa).
$\sigma_{\theta,T=1.5T_m}^{1.5P(0)\sim 1.5P(4\pi)}(\theta)$	interface stress σ_θ under impact force $T = 1.5T_m$ due to the load $P = 1.5P_0$ moves two rotations (MPa).
σ_θ^{Res}	residual stress (MPa).
$\sigma_\theta^{Rolling}$	rolling stress (MPa).
$\sigma_\theta^{Res+Shrink}$	sum of residual stress and shrink-fitting stress (MPa).
σ_{w0}	DCI alternate fatigue strength (MPa).
φ	load shift angle (°).
φ_0	load shift interval (°).
l_b	slip distance (mm).
ℓ_s	slip distance (mm).
ℓ_{total}^{sleeve}	slip defect length on the sleeve (mm).
ℓ_{total}^{shaft}	slip defect length on the shaft (mm).
a, b, c	dimension of the defect in the miniature roll (μm).
r, θ, z	polar coordinate system.
x, y, x	cartesian coordinate system.

in ball/roller bearing, the slip will be verified under free rolling. Note that, even when there is no shrink-fitting of $\delta/d = 0$, the sleeve and the shaft managed to be in contact with each other due to the load P in Fig. 1. Hence, the shrink-fitting ratios of $\delta/d = 0$ and $\delta/d = 0.21 \times 10^{-3}$ will be considered in this study.

To verify the numerical simulation and to gain a deeper understanding of the interfacial slip phenomenon, the formation and the growth of slip defects will be clarified by observing the slip surface in detail. In addition, the shape and dimensions of the slip defect finally formed on the shrink-fit surface will be identified, and the stress concentration will be taken into consideration to evaluate the fatigue strength of the sleeve roll. In this way, in this research, the mechanism of interfacial slip of the rolling sleeve roll will be elucidated, and countermeasures and strength evaluation will be performed. In addition, in order to develop next-generation rolls such as super cermet rolls and all-ceramic rolls, it is necessary to adopt a sleeve roll structure that shrink-fits the sleeve and shaft, so application to them can be expected.

2. Experimental verification of interface slips by using a miniature rolling mill

2.1. Experimental conditions and methods

Fig. 1a shows a hot rolling mill testing machine that was developed by Hitachi Metals. Table 1 shows the specifications of the miniature roll testing machine [38]. This testing machine is used to evaluate surface roughness and weariness of the work roll by passing the hot coil between the upper and lower work rolls. However, in this research, a pair of the work rolls are driven by a direct contact without the passing of hot coil to realize the slip under free rolling. Fig. 1b illustrates the roll configuration and the position of the test roll in the rolling stand from the driving side. In this experiment, the upper work roll is the target roll

without any driven state. The target work roll is driven by the contact force from the lower pair roll and also in touch with the upper back-up roll, which is supported by a roller bearing. Note that, the contact effect of the back- up roll is small and negligible. The target roll has a double shaft structure whereby the inner and the outer shafts are fixed with a key to realize the circumferential slip at the shrink-fitting interface between the sleeve and the outer shaft (see Fig. 3c). SCM440 material was used for both the sleeve as well as the shaft.

Table 2 shows the specifications of the test work roll. The diameter of the test roll is about 1/10 of the diameter of the real roll. Table 3 displays the experimental conditions. Roll A denotes the roll without the shrink-fitting ratio of $\delta/d = 0$ and roll B denotes the roll with the shrink-fitting ratio of $\delta/d = 0.21 \times 10^{-3}$. In the experiment, the work roll is cooled with water at room temperature to prevent the change in shrink-fitting rate due to the temperature rise caused by friction due to the load. When the steady rotation speed reached 106 rpm or 212 rpm, a load of 1 ton is applied to ensure that the temperature change of the roll surface is within 5℃ or less during the experiment by a contact thermometer.

2.2. Experimental results for interface slip

Fig. 2a illustrates the slip status of roll A specimen with no shrink-fitting of $\delta/d = 0$. The slip distance $\ell_s = \pi d\theta_{slip}/360$ can be obtained as relative circumferential movement from the scribed lines as shown in Fig. 2a, before and after the experiment. The slip angle $\theta_{slip} = 76^\circ$ specifying the slip distance $\ell_s = \pi d\theta_{slip}/360 = 31.8$ mm which occurs after the number of the roll rotation $n = 1 \times 10^4$. Fig. 2b illustrates the slip status of roll B specimen of $\delta/d = 0.21 \times 10^{-3}$. Fig. 2b shows the slip angle $\theta_{slip} = 77^\circ$ specifying the slip distance $\ell_s = \pi d\theta_{slip}/360 = 32.3$ mm which occurs after the number of the roll rotation $n = 3 \times 10^4$.

In the previous study, the numerical simulation was performed to realize the circumferential slip in shrink-fitting sleeve roll (see Appendix A). The rotation of the roll was replaced by load shifting $P(0) \sim P(\varphi)$ with load shift angle φ on a fixed roll surface. Afterwards, the interfacial displacement $u_\theta^{P(0)\sim P(\varphi)}(\theta)$ in the θ-direction was obtained [20–23]. In the next section, the notation $u_\theta^{P(0)\sim P(\varphi)}(\theta)$ is illustrated as shown in Fig. 4. For instance, when the number of roll rotation is n, the non-uniform slip can be expressed as $u_\theta^{P(0)\sim P(2n\pi)}(\theta)$ by putting $\varphi = 2n\pi$.

Table 1
Specifications of the miniature roll testing machine.

Roll size	Back-up roll size (Body diameter D_B × Body length) (mm)	120 × 40
	Back-up roll material	SCM440 Quenched and tempered
	Work roll size (Body diameter D_B × Body length) (mm)	60 × 40
Specification	Load P (ton)	~ 10
	Rotating speed (rpm)	1150
	Driving system	Work roll drive (Two rolls / One motor)
	Driving motor	Speed 3-phase induction motor
	Power (kW), Pulse speed (Hz)	55, 59.2
	Voltage (V), Current (A)	180, 225
	Coil tension force (MPa)	100 ~ 1000
	Coolant: Front (L/min), Back	~ 1.0, ~ 4.5
	Rolled coil size (mm), Material	$1 \times 15 \times (250 \times 10^3)$ (Thickness×Width×Length), Steel

Table 2
Test work roll specifications (see Fig. 3b).

Specifications	
Size D, d, d_1 (mm)	60, 48, 35
Material	SCM440 Quenched and tempered
Tensile strength σ_B (N/mm^2)	980
Hardness HB	Sleeve: 280 ~ 300 Shaft: 305 ~ 330

Since $u_\theta^{P(0)\sim P(\varphi)}(\theta)$ slightly varies depending on θ, the average value $u_{\theta,ave.}^{P(0)\sim P(2n\pi)}$ was defined in the previous paper as shown in Eq. (1) (see Fig. A2).

$$u_{\theta,ave.}^{P(0)\sim P(\varphi)} = \frac{1}{2\pi}\int_0^{2\pi} u_\theta^{P(0)\sim P(\varphi)}(\theta)d\theta \quad (1)$$

(numerical simulation) $\approx \ell_s$(experiment)

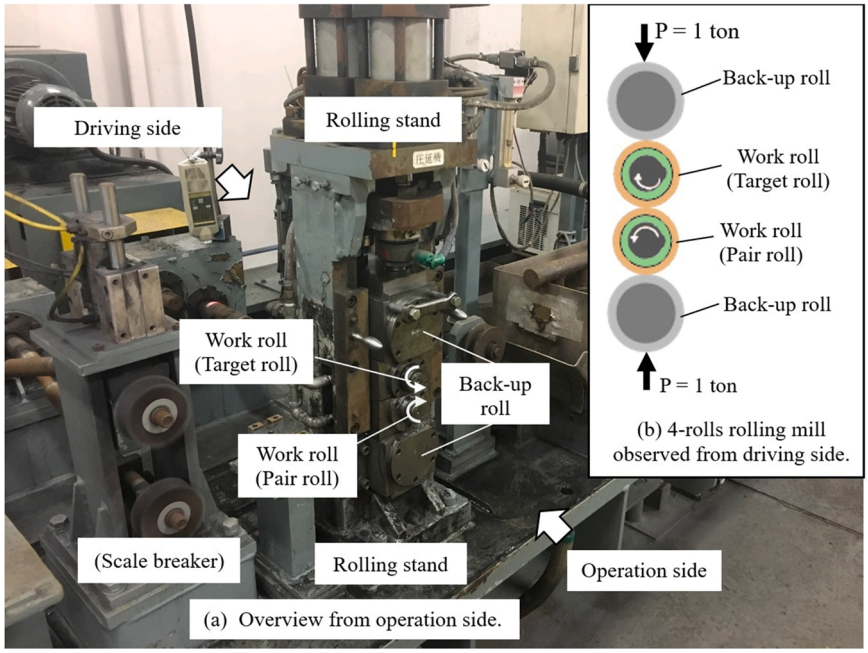

Fig. 1. Miniature rolling mill whose size is about 1/10 of the real rolling mill.

Table 3
Experimental conditions.

Test roll	Shrink fitting ratio δ/d	Roll A	0
		Roll B	0.21×10^{-3}
Driving condition	Test roll		Free rolling
	Pair roll		Driven by the torque 457 Nm
	Load P (ton)		1.0
	Rotating speed (rpm)		106 ~ 212
	Roll cooling: Front side (L/min), Back side		Water 0.25, 2.0
	Roll temperature (°C): δ/d= 0.21 × 10^{-3}, 0		16.0 ~ 21.0
	Number of rotations, n		Rotations until sleeve slip

This average displacement $u_{\theta,ave.}^{P(0)\sim P(\varphi)}$ obtained by the numerical simulation is corresponding to the slip distance ℓ_s experimentally obtained as indicated in Eq. (1). The previous simulation showed the average displacement $u_{\theta,ave.}^{P(0)\sim P(\varphi)}$ was initially unstable but became stable from after one rotation [23]. The slip distance per rotation ℓ_s/n can be expressed as shown in Eq. (2).

$$\ell_s \Big/ n \text{ (experiment)} = \frac{\theta_{slip}\pi d}{360 \bullet n} \approx u_{\theta,ave.}^{P(0)\sim P(2n\pi)} \Big/ n \text{ (numerical } simulation\text{)} \tag{2}$$

In the numerical simulation, the displacement increase rate $du_{\theta,ave}^{P(0)\sim P(2n\pi)}/d\varphi$ was highlighted as well. In particular, it was found that $du_{\theta,ave}^{P(0)\sim P(2n\pi)}/d\varphi$ becomes almost constant after one rotation of the roll [23]. The displacement increase rate $du_{\theta,ave}^{P(0)\sim P(2n\pi)}/d\varphi$ can be expressed experimentally as similar as the slip distance per degree shown in Eq. (3).

$$du_{\theta,ave.}^{P(0)\sim P(2n\pi)} \Big/ d\varphi \text{ (numerical simulation)} \approx \frac{\theta_{slip}\pi d}{360 \bullet 360n} \text{ (experiment)} \tag{3}$$

Note that those Eqs. (2) and (3) are based on the assumption that the slip occurs consistently during the roll rotation. Table 4 summarizes the slip distance experimentally obtained ℓ_s, total number of rotations of the roll $(n_t - n_0)$, the slip distance per rotation $\pi d\theta_{slip}/(360\cdot(n_t - n_0))$, and the displacement increase rate $\pi d\theta_{slip}/(360^2\cdot(n_t - n_0))$. Table 4 indicates that the slip distance per rotation $\pi d\theta_{slip}/(360\cdot(n_t - n_0))$ of roll A is nearly three times larger than the ones of roll B as well as the displacement increase rate $\pi d\theta_{slip}/(360^2\cdot(n_t - n_0))$.

3. Numerical simulation for an interfacial slip in the miniature roll

3.1. Outline of numerical simulations

Fig. 3a and b illustrate the central cross section of the real roll in comparison with the central cross section of the miniature roll. Fig. 3c shows the load shifting method to realize the slip. In the miniature sleeve roll in Fig. 3b, the inner shaft and the outer shaft are fixed by using a key so that the slip does not occur at the interface. Instead, the outer shaft and the sleeve are assembled by shrink-fitting so that the interfacial slip may be realized. In a real roll, in order to meet the demand for the high wear resistance and high toughness, bimetallic sleeve is commonly used for the rolling roll. Therefore, wear-resistant material such as high-speed steel or high-chrome steel is used for the outer layer, and alloy steel is used for the inner layer. In the miniature roll experiment, however, a steel sleeve and a steel shaft are used. Table 5 shows the detail of the sleeve properties, inner and outer shafts, as well as the keys. As shown in Fig. 3 c, the roll rotation is fixed by introducing a rigid body at the roll center.

Fig. 4 illustrates the relative displacement $u_{\theta}^{P(0)\sim P(\varphi)}(\theta)$ due to the shifted load $P(0) \sim P(\varphi)$ in Fig. 3. As shown in Appendix A [20–23], the load shifting method is applied to investigate the non-uniform slip for the miniature roll specimen. In this study, to clarify the interfacial slip

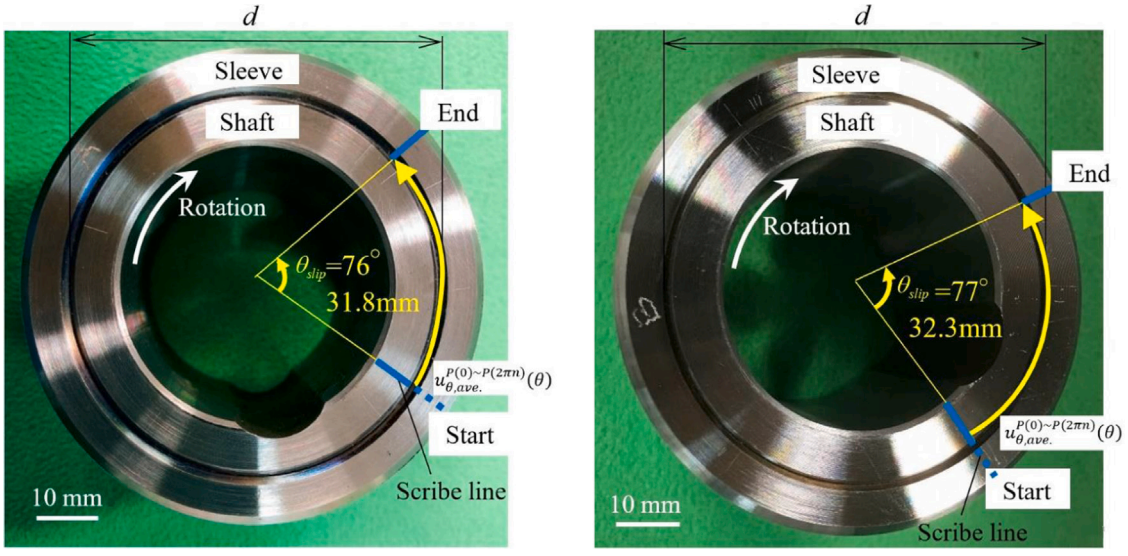

(a) Roll A of $\delta/d = 0$ at n = 1×10^4. (b) Roll B of $\delta/d = 0.21 \times 10^{-3}$ at n = 3×10^4.

Fig. 2. Experimentally obtained slip angle θ_{slip} of the target roll in Fig. 1 observed from driving side. The slip distance $\ell_s = \pi d\theta_{slip}/360$ can be experimentally obtained from the slip angle θ_{slip}. In the numerical simulation, the slip distance is obtained as the relative displacement as $\ell_s \approx u_{\theta,ave.}^{P(0)\sim P(2n\pi)}(\theta) = u_{\theta,Sleeve}^{P(0)\sim P(2n\pi)}(\theta) - u_{\theta,Shaft}^{P(0)\sim P(2n\pi)}(\theta)$ with n = number of rotation.

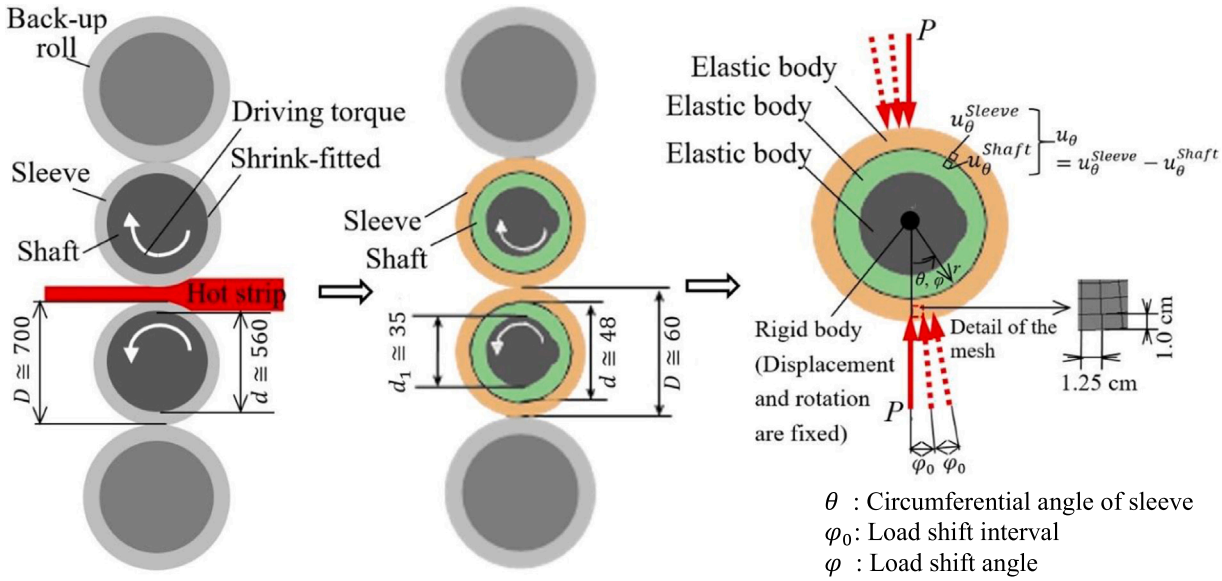

(a) Real roll with motor torque at the central cross section

(b) Miniature roll under free rolling

(c) Modelling of the target work roll

Fig. 3. Schematic illustration for (a) Real roll with motor torque at the central cross section, (b) Miniature roll under free rolling (c) Modelling of the target work roll.

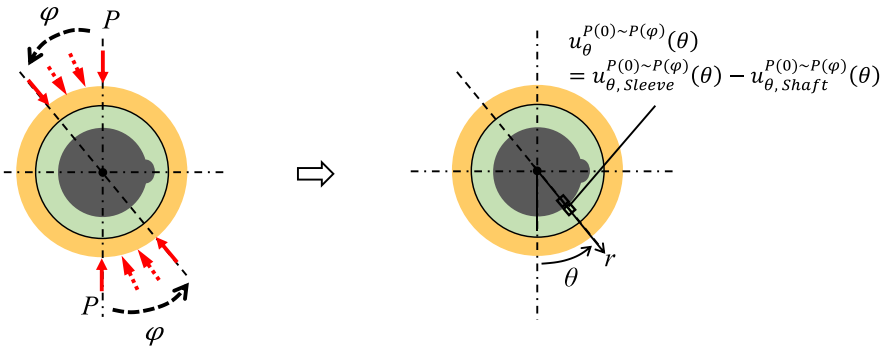

(a) Define the pair of the loads shift from $\varphi = 0$ to φ, and $\varphi = \pi$ to $(\pi + \varphi)$ as $P(0) \sim P(\varphi)$.

(b) Define the displacement $u_\theta(\theta)$ due to $P(0) \sim P(\varphi)$ as $u_\theta^{P(0)\sim P(\varphi)}(\theta)$.

Fig. 4. Definition of the relative displacement $u_\theta^{P(0)\sim P(\varphi)}(\theta)$ due to the shifted load $P(0) \sim P(\varphi)$ for the miniature roll specimen in Fig. 3.

Table 4
Experimentally obtained relative slip distance ℓ_s and relative displacement per rotation ℓ_s/n.

Shrink-fitting ratio δ/d	Relative slip distance $\ell_s = \frac{\pi d\theta_{slip}}{360}$ (mm)	Number of rotations $n_t - n_0$	Relative displacement per rotation $\frac{\pi d\theta_{slip}}{360(n_t - n_0)}$ (mm/rev.)	Displacement increase rate $\frac{\pi d\theta_{slip}}{360^2(n_t - n_0)}$ (mm/deg.)
Roll A $\delta/d = 0$	31.8	1×10^4	3.18×10^{-3}	8.84×10^{-6}
Roll B $\delta/d = 0.21 \times 10^{-3}$	32.3	3×10^4	1.08×10^{-3}	2.99×10^{-6}

generation, free rolling is applied to both work roll and back-up roll. Presumably, the shaft rotation torque $T = 0$ and the frictional force which is due to the rolled material $S = 0$. Fig. 5 shows the FEM mesh with the dimension for the target roll having a double shaft structure whereby the inner shaft and the outer shafts are fixed with a key so that the slip may appear only at the shrink-fitted interface between the sleeve and the outer shaft. SCM440 material is used for both of the sleeve and the shaft. In this analysis, similar to the miniature roll experiment, the load $P = 245$ N/mm is applied from the back-up roll to the sleeve as well as the reaction force from the rolled plate to the sleeve [22]. The

Table 5
Analytical condition in the miniature roll.

Property		
	Sleeve	
	Young's modulus of steel sleeve E (GPa)	210
	Poisson's ratio of steel sleeve ν	0.28
	Shaft	
	Young's modulus of shaft E_s (GPa)	210
	Poisson's ratio of shaft ν_s	0.28
Roll size	Outer diameter of sleeve D (mm)	60
	Inner diameter of sleeve d (mm)	48
Shrink-fitting	Shrink-fitting ratio δ/d	0.21×10^{-3}
	Friction coefficient between sleeve and outer shaft μ	0.3
External force	Concentrated load per unit width P (N/mm)	245 (Total: 1 ton, Rolled width: 40 mm)
	Frictional force per unit width S (N/mm)	0
	Bending force from bearing P_b (Nm/mm)	0

shrink-fitting ratio is defined as δ/d which is composed from the shrink-fitting allowance δ and the inner diameter d. Here, $\delta/d = 0.21 \times 10^{-3}$ is used in the miniature roll analysis. The friction coefficient between the sleeve and the outer shaft is $\mu = 0.3$. In the manufacturing procedure, firstly, the inner diameter of the sleeve is machined, and the shaft is shrink-fitted into the sleeve. Secondly, the inner diameter of the shaft is machined including the keyway. Finally, the inner shaft is fixed into the inner diameter by the key. The tightening allowance is $\delta = 0$ mm for roll A and $\delta = 0.01$ mm for roll B. The shrink-fitting ratios are $\delta/d = 0$ and $\delta/d = 0.21 \times 10^{-3}$ for roll A and roll B respectively.

3.2. Comparison of slip distance obtained by the analysis and the experiment

In this study, the miniature roll experiment in Fig. 1 is conducted to verify the simulation results. Fig. 5 illustrates the target work roll expressed as FEM mesh whose diameter is 60 mm used. As shown in Table 3, the experiment is conducted under free rolling with no motor torque because a similar phenomenon known as "interfacial creep" in ball bearing [22]. To realize the slip between sleeve and shaft in Fig. 5, the outer shaft and the inserted inner shaft are fixed by the key. In the experiment, the work roll is cooled down by water at room temperature to prevent the change of the shrink-fitting ratio due to rising temperature. Under the steady rotation, the load of 1 ton is applied confirming the roll surface temperature change was within 5 °C or less during the experiment by a contact thermometer.

The FEM simulation is performed by using the mesh in Fig. 5. Four-node quadrilateral plane strain elements are used, and the total number of mesh elements is 7408 [44]. By assuming the loading $P = 245$ N/mm, the shrink-fitting ratio $\delta/d = 0.21 \times 10^{-3}$ and the constant friction coefficient $\mu = 0.3$ between sleeve and shaft, the numerical simulation is newly performed for the miniature roll. Similar to Fig. A.2b, $u_\theta^{P(0)\sim P(\varphi)}(\theta)$ is defined as the relative displacement between sleeve and shaft.

Table 6 compares the experimental results and the numerical simulation results regarding the displacement increase rate $du_{\theta,ave.}^{P(0)\sim P(2n\pi)}/d\varphi$ and the slip distance $\ell_s = \frac{\pi d\theta_{slip}}{360} \approx u_{\theta,ave.}^{P(0)\sim P(2n\pi)}$. The simulation results in Table 6 are based on the assumption where the slip appears at the same time when the roll rotation starts, and consistently appears throughout the roll rotation without causing the slip defect. From Table 6, it is seen that the simulation results are 3.6 ~ 4.3 times larger than the experimental results. This difference can be explained from a constant friction coefficient $\mu = 0.3$ assumed in the simulation, even though the friction coefficient is kept changing like $\mu = 0.3 \sim \infty$ throughout the experiment due to the growth of the slip defect. In the experimental observation, due to the circumferential slip, slip defects start with thin and shallow scratches, then, they become thicker and deeper with erosive wear and cohesive wear, and eventually form large defects that completely stop

Table 6
Comparison of the experimental results and the simulation results.

Shrink-fitting ratio δ/d	Displacement increase rate $\frac{du_{\theta,ave.}^{P(0)\sim P(2n\pi)}}{d\varphi} \approx \frac{\pi d\theta_{slip}}{360^2(n_t - n_0)}$ (mm/deg.)		Relative displacement $u_{\theta,ave.}^{P(0)\sim P(2n\pi)} \approx \ell_s = \frac{\pi d\theta_{slip}}{360(n_t - n_0)}$ (mm/rev.)	
	Experiment (mm/deg.)	Simulation (mm/deg.)	Experiment (mm)	Simulation (mm)
Roll A $\delta/d = 0$	0.884×10^{-5}	3.074×10^{-5}	0.318×10^{-2}	1.356×10^{-2}
Roll B $\delta/d = 0.21 \times 10^{-3}$	0.299×10^{-5}	1.103×10^{-5}	0.108×10^{-2}	0.384×10^{-2}

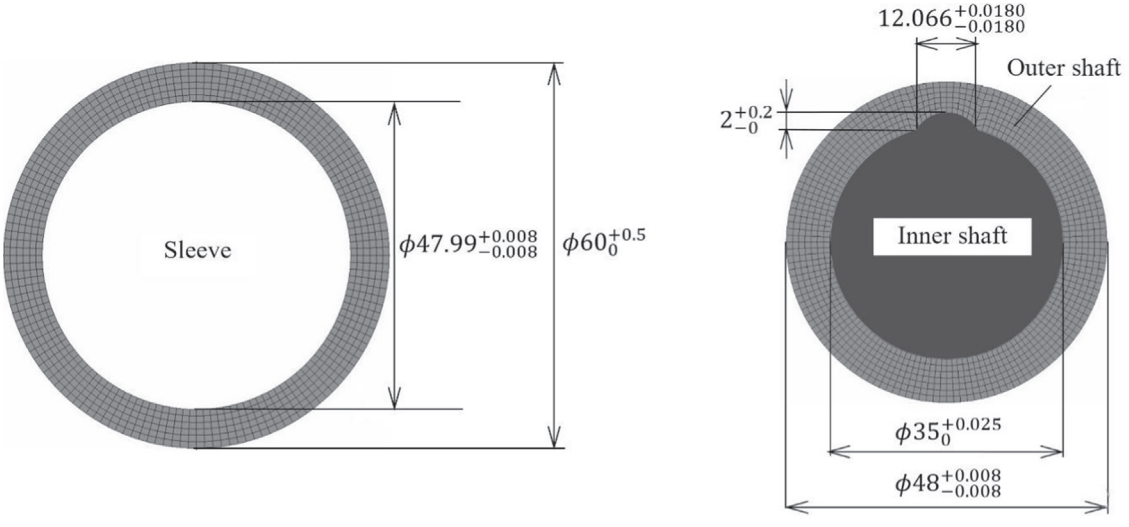

(a) Sleeve (b) Shaft

Fig. 5. Dimensions of the miniature target work roll specimen in Fig. 1 expressed as FEM mesh when $\delta/d = 0.21 \times 10^{-3}$.

the slip. In the simulation, the constant friction coefficient $\mu = 0.3$ should be changed to $\mu = 0.3 \sim \infty$, but actually the change reflecting the real defect evolution is almost impossible in practice. This is the reason why 3.6 ~ 4.3 times difference appears between the experiment and the simulation. Although the results are comparatively larger, the current simulation can still be used for comparative purposes. For example, both experiment and numerical simulation showed that the results under no shrink-fitting of $\delta/d = 0$ are 2.79 ~ 3.53 times larger than the results of $\delta/d = 0.21 \times 10^{-3}$. The following section explains the slip defect observed in the sleeve and shaft surfaces that are studied comprehensively.

4. Slip defects caused by an interfacial slip in miniature roll

4.1. Observation on the sleeve surface

A detailed observation is performed for the damaged surface of roll B with $\delta/d = 0.21 \times 10^{-3}$ since the real sleeve roll is shrink-fitted. Fig. 6 shows the entire circumferential surfaces of (a) the inner surface of the sleeve and (b) the outer surface of the outer shaft (hereinafter referred to as the shaft). Four slip defects are observed on the sleeve surface as well as shaft surface, and the four defects in Fig. 6a are the same of the four defects in Fig. 6b. Those four slip defects are denoted by ①, ②, ③, ④. Here, the slip defect ② is focused since the defect size ② is relatively the largest.

Fig. 7 illustrates the enlarged views of the slip defect ② in Fig. 6a. As indicated in Fig. 7a, the entire defect can be classified into several regions. To express the characteristic of those regions, the term "slip defect" is used for the entire region. On the other hand, the term "scratch" is used only at the earliest region. Moreover, the term "an ellipsoidal defect" is used at the end of the region. At the starting point of the defect in Fig. 7a, some scratches with intermittent white lines are seen along with a pitch corresponding to the feed amount of the tool. Then, the slip defect is developed by erosion wear and cohesive wear during the rolling. Finally, the slip defect forms a comparatively larger ellipsoidal defect at the end of the defect since the slip is stopped.

In this way, the defect growing process can be classified into Region 1 ~ Region 5. Firstly, as shown in Fig. 7b, Region 1 includes intermittent white lines caused by scratch wear. Due to the high-pressure contact at the top of the machined surface, the slip defect starts with the scratch at the top of roughness as arcuate protrusions. Secondly, in Region 2 in Fig. 7b, those grooves between the white lines merge into a thick linear defect repetitively and gradually become thicker and glossy blackish grooves. From the analysis, this linear groove is formed due to the combined actions of the scratch wear, the adhesive wear, and the erosive wear. As shown in the enlarged view in Fig. 7b, spheroidal particles can be seen in the grooves. This is a characteristic phenomenon that occurs when a slip is repeatedly applied under high-pressure, and is also a characteristic of the adhesion wear phenomenon [41]. The spherical particles are in a strong bonded state because the wear debris sticks and adheres to each other by reciprocating motion under high-pressure. In the middle of Region 2, an elliptical shaped defect with black fragmentary grooves surrounded by white dashed line frame can be seen in Fig. 7b. This is a trace formed during the period when the slip was stopped for a relatively long time. More details will be shown in the upcoming Region 5 since a similar elliptical defect is seen in Region 5. In Region 3, Fig. 7c portrays the width of the defect that becomes larger. This width extension is caused by the coalescence of another slip defects as shown in Fig. 7c. Fig. 7d shows that, Region 4 includes irregular shaped grooves during the defect's width growth, unlike from other regions previously described. It may be conjectured that those irregular shaped grooves were caused by an erosive wear affected by the loss of the slip direction as the slip speed becomes slower. Note that there are signs of erosive wear existed even before Region 3.

Fig. 7e shows the Region 5 part where the slip eventually remained. It is seen that the defect has reached the maximum depth, which will be further described later in Fig. 12. This state including the maximum depth can be regarded as the final point of the defect. At this position, due to the stopping of the slip, cohesive wear occurs throughout the entire Region 5. Therefore, in Region 5, the cohesive particles are less

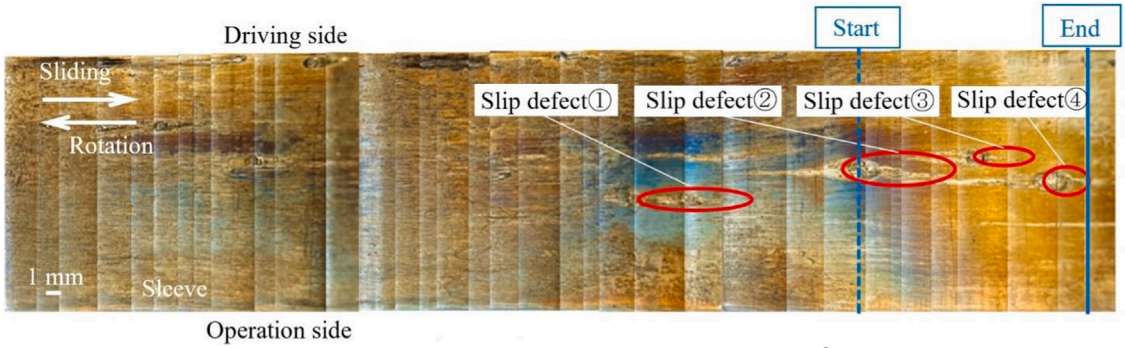

(a) Sleeve surface of roll B, $\delta/d = 0.21 \times 10^{-3}$.

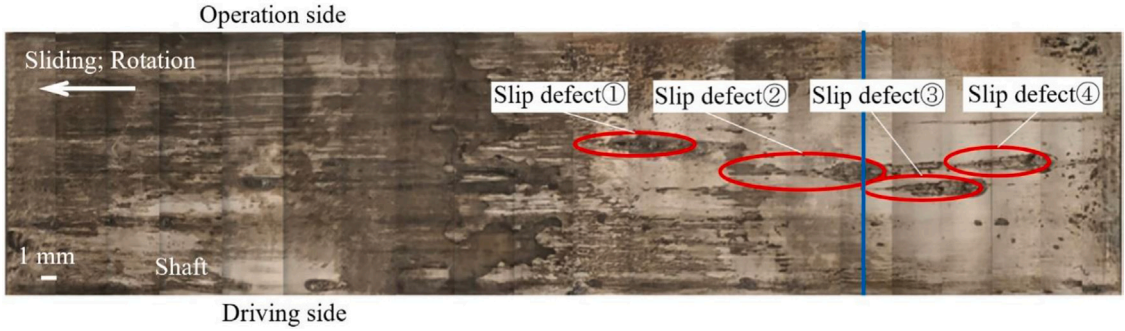

(b) Shaft surface of roll B, $\delta/d = 0.21 \times 10^{-3}$.

Fig. 6. Slip defects denoted by ①, ②, ③, ④ observed on the (a) sleeve surface and (b) shaft surface.

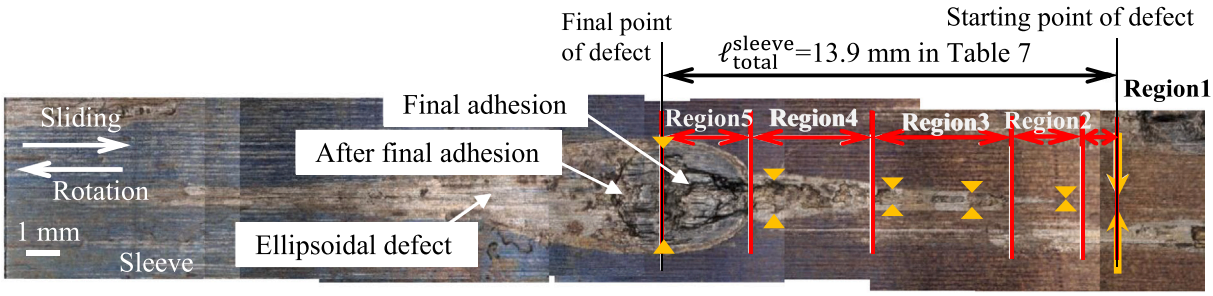

(a) Slip defect ② which can be classified into Region 1~Region 5 on the sleeve surface.

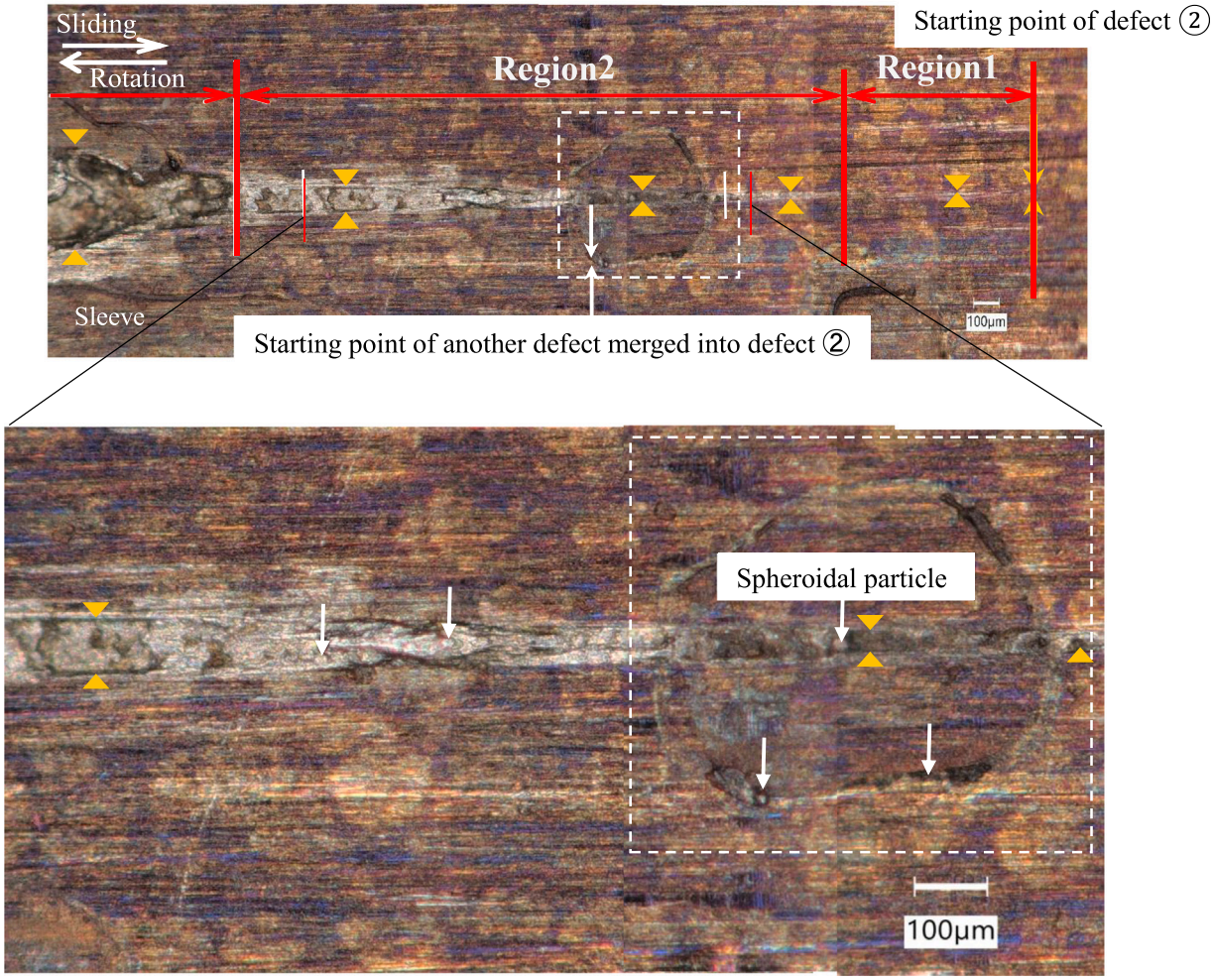

(b) Enlarged view of Region 2 of slip defect ② on the sleeve surface.

Fig. 7. Slip defect ② whose whole region can be classified into Region 1~Region 5 on the sleeve surface.

likely to be discharged. Furthermore, due to the repetition of the compressive force acting at each rotation, the adhesion of wear products progresses mainly inside the groove. At the same time, the slippage stops due to an increase in slip resistance which is caused by the widening of the groove. A slope is observed at the final position of Region 5. After a certain period of non-slip phenomenon, an elliptical trace of the entire Region 5 is formed in a similar way as the ellipse generation in Region 2. The reason behind the forming of this trace can be explained in the following way. The cooling water drawn into the widened black groove is diffused to the surroundings during compression, and the cooling

(c) Enlarged view of Region 3 of slip defect ② on the sleeve surface. (Another slip defect to be united can be seen in Region 2.)

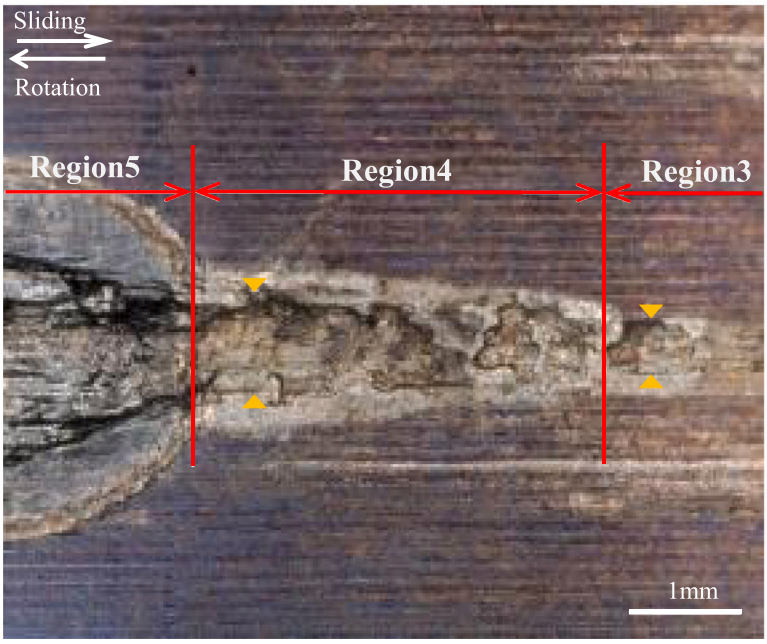

(d) Enlarged view of Region 4 of slip defect ② on the sleeve surface.

Fig. 7. (*continued*).

water is drawn in after decompression. This action is repeated for each roll rotation. Due to the repeated compressive force, the inside surface of the black groove began to crush. On top of that, the cohesive wear of the crushed particles inside of the black groove occurs in the depth direction and progresses to the deepest direction. Several irregular shapes which were formed due to the crush led to the increase in generating a gap between the sleeve and shaft, and preventing the contact by the apparent volume of the cohesive particles. With the increase in the distance from the groove, the gap becomes smaller, and a contact condition is formed where the short radius is 1.7 mm from the elliptical trace (on the outer circumference of the elliptical trace). Eventually, the elliptical erosive groove is formed at the contact portion due to the inflow and outflow of high-pressure and high-speed water.

In Fig. 7e, the semicircular area at the left front of Region 5 was originally a normal wear surface with no defect when the slippage stopped. However, it was then changed to the slip defect like surface after a certain period of non-slip. The surface change is caused by an accumulation of the erosive wear and adhesion wear due to the drawing in and out of the cooling water under repeated compressive force. A similar pattern can be seen in Region 5 on the shaft surface.

4.2. *Observation on the shaft surface*

Fig. 8a illustrates the enlarged views of slip defect ② in Fig. 6b on the

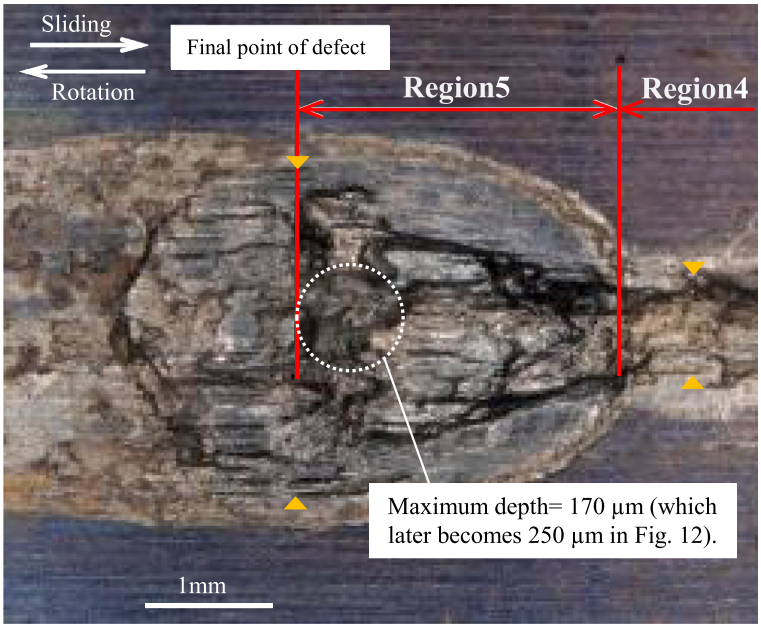

(e) Enlarged view of Region 5 of slip defect ② with the maximum depth 250 μm on the sleeve surface. (The semicircular region at the left front of Region 5 was originally a normal wear surface and changed to the slip defect like surface after a certain period of non-slip).

Fig. 7. (*continued*).

shaft surface. As indicated in Fig. 8a, the entire defect on the shaft is classified into Region 1 ~ Region 5, which is similar to Fig. 7a on the sleeve. From Fig. 8a, it can be seen that Region 1 contains worm-eaten like erosive wear and intermittent white lines indicating scratch wear. In addition, the discoloration range that looks like an oxide film is partially widened. In Region 2, although it is quite unclear, a series of continuous grooves can be seen and the width is gradually increasing. The groove is shallow, and white flakes are scattered on the bottom of the groove, and the boundary of the grooves is also unclear. In Region 3, the groove width is further widened, and no difference can be seen between the state where white flakes are scattered and its surroundings. In Region 4, as shown in Fig. 8b, the groove width suddenly expands. The inner surface is blackish and glossy, and the partial boundary becomes clear. Nonetheless, glossy grooves with worm-eaten like erosive wear can also be seen irregularly, and the partial groove boundary is unclear. Region 5 is where the slip eventually stopped, and the position of the stop end coincides with the sleeve. Similar to the sleeve, an elliptical shape trace can be seen around the boundary (see Fig. 8a and b). During non-slip, due to the repeated contact, worm-eaten like erosive wear spreads further as shown in Fig. 8c. Compared to Region 3, white flakes in Region 5 are also observed. Although they are not uniformly dispersed as in Region 3 but are unevenly distributed under the influence of adhesive wear. In the semicircular region situated at the right front of Region 5 in Fig. 8a, the maximum height of 170 μm can be seen as shown in Fig. 8d. Such height and depth of the defect is measured by using digital microscope (VHX-970 F KEYENCE) usually after cutting the specimen whose detail will be described later in Section 5.1 regarding the defect on the sleeve surface. It should be noted, the maximum depth of the defect on the sleeve discovered is 170 μm, which later becomes 250 μm around the same area (see Figs. 7e and 12). The cohesive mass is generated on the sleeve side, which has lower hardness, sticks to the shaft side, and swells to reach the maximum height. It is conjectured that the cohesive mass is formed by applying a repeated compression load to the wear debris which was generated on the sleeve side after the slip stops.

In Sections 4.1 and 4.2, the slip defect ② was observed on the sleeve and the shaft were classified into Region 1 ~ Region 5. From there, the characteristics and changes of those regions were described, leading to the clarification of the defect formation and growth. Similarly, slip defect ④ can be classified into Region 1 ~ Region 5 and its growth process can be traced as discussed for Figs. 7 and 8.

4.3. *Adhesive wear model for Region 1 and Region 2*

The adhesion wear generation for Region 1 and Region 2 can be explained by using a model proposed by Sasada as shown in Fig. 9 [39]. Fig. 9 illustrates the growth and detachment process of the transferred particles when two opposite surfaces move relatively. In Fig. 10, the particles before falling off are illustrated as the wear particles at friction interface. The process can be summarized in the following way.

(1) The real contact portions, which are the protrusions on the surface, come into contact and deform to form junctions.
(2) The formed junctions are sheared and broke out from the inside of the material.
(3) The broken part adheres to the contact surface and generates a transfer element, which is an elementary particle that forms a wear particle.
(4) Adhesive particles which are generated on a mutual friction surface aggregate, merge at the friction interface, and grow to form transferred particles.
(5) Finally, wear occurs when the transferred particles are fallen off and released from the friction surface as wear particles.

According to this model, the transferred particles are crushed and spread by frictional force while supporting the load at the friction interface. In this way, the defect caused by interfacial slip begins with a scratch wear at the top of the finishing process. In regard to this, the starting point of the adhesive defect of the sleeve shown will be identified accurately to determine the defect length in the next Section 4.4.

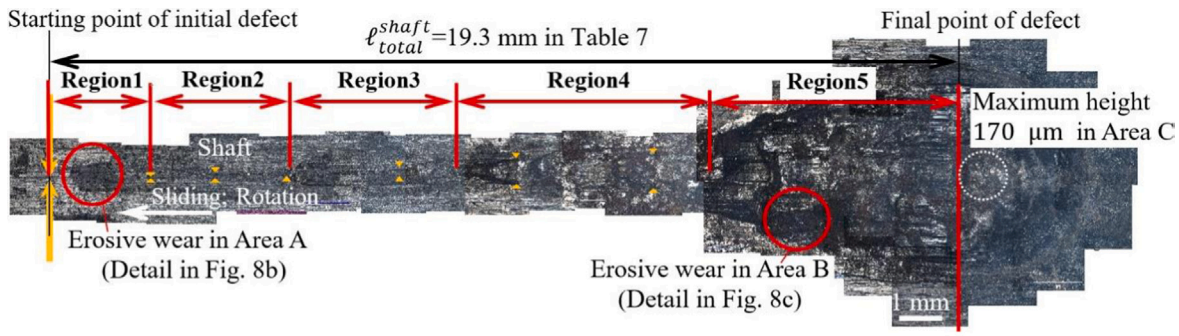

(a) Slip defect ② on the shaft surface consisting of Region 1~Region 5.

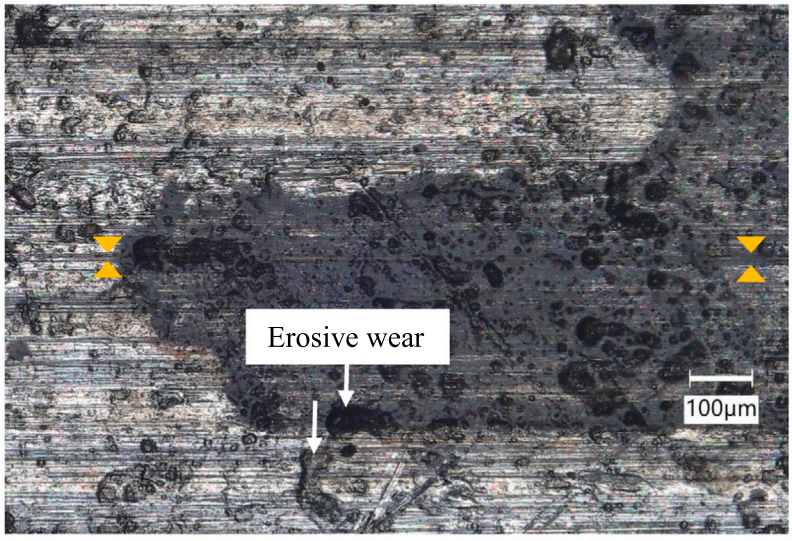

(b) Erosive wear in Area A in Region 1 of slip defect ②.

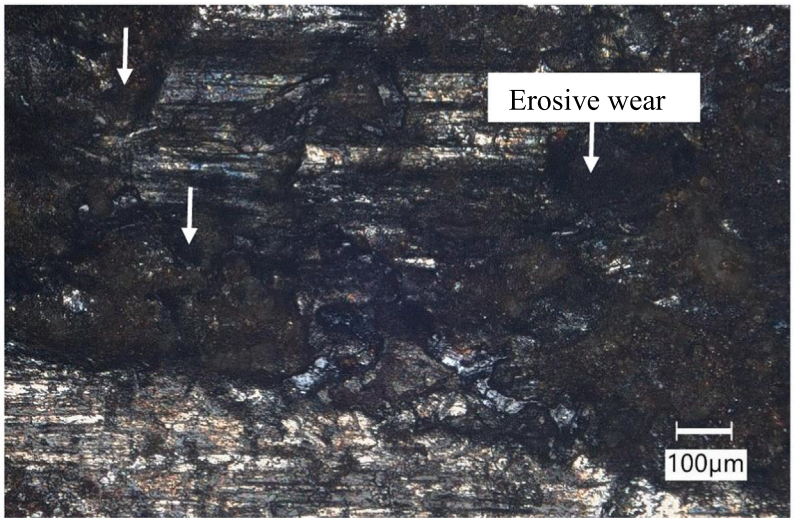

(c) Erosive wear in Area B in Region 5 of slip defect ②.

Fig. 8. Slip defect ② whose whole region can be classified into Region 1~Region 5 on the shaft surface.

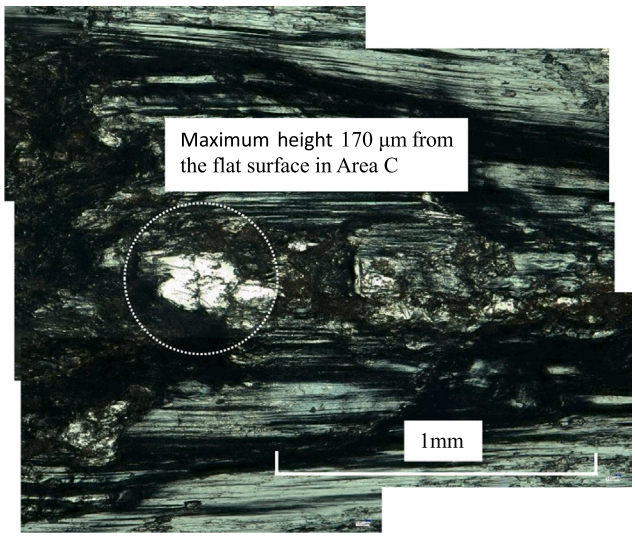

(d) Maximum height 170 μm (see Fig. 12) in Area C in the right front of Region 5 of slip defect ②.

Fig. 8. (*continued*).

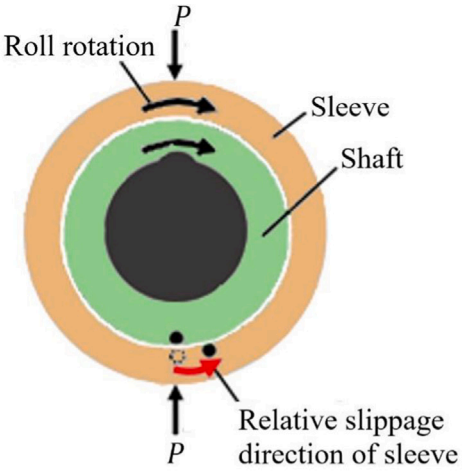

(a) 4-rolls rolling mill

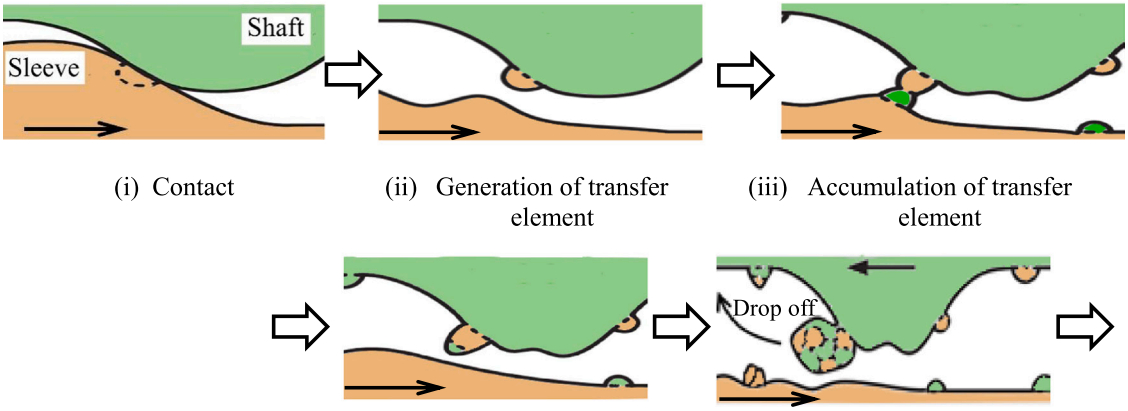

(b) Detail of transfer particles formation process of Area C from Fig. 8a.

Fig. 9. Sasada's model of transfer particles and growth during sliding to explain the change from Region 1 to Region 2.

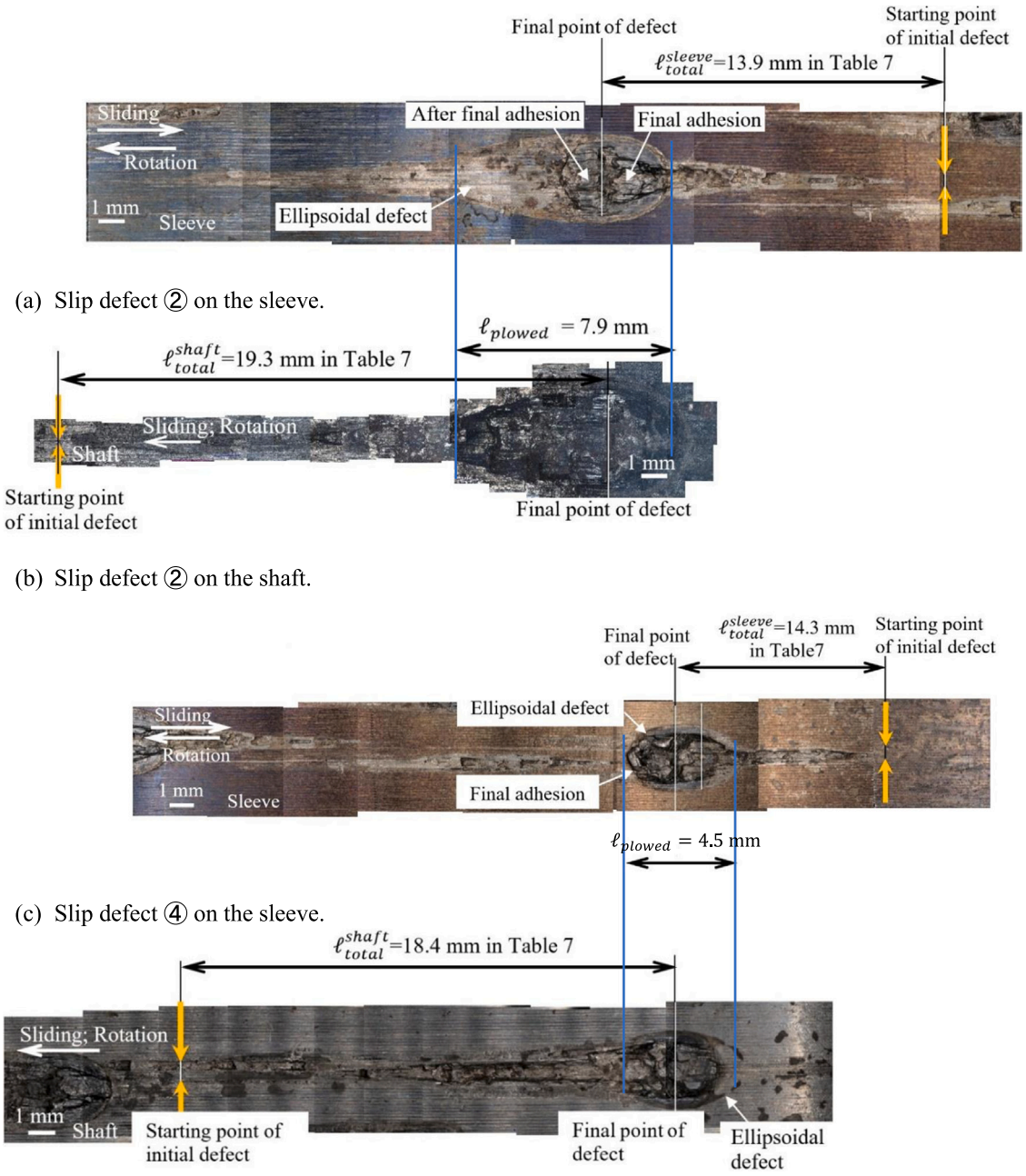

Fig. 10. Slip defects ② and ④ on the sleeve and shaft.

4.4. Defect length in relation to the slip distance

In this section, the defect length on the sleeve and shaft surface are considered. The slip starts with the roll rotation, and the starting point corresponds to the scribe line on the miniature roll specimen in Fig. 2. Due to the relative slip between the sleeve and shaft, the sleeve slip of the length ℓ_{total}^{sleeve} occurs in the direction which is opposite to the rotation with respect to the shaft. Instead, the shaft slip of the length ℓ_{total}^{shaft} occurs in the same direction as the rotation direction. The sum $\ell_{total}^{sleeve}+\ell_{total}^{shaft}$ is compared with the slip amount $\ell_s = \pi d\theta_{slip}/360$ in Fig. 2 that is obtained from the scribe line in the miniature roll specimen. The relationship between the slip distance ℓ_s and the slip defect length in Fig. 6 is discussed by observing the slip defects ② and ④ in detail since the defect size ② and ④ are relatively the largest.

Fig. 10 shows the slip defects ② and ④ on the sleeve and shaft were observed at 50× magnification. As shown in Fig. 10a and b, the slip defect ② has ℓ_{total}^{sleeve} = 13.9 mm on the sleeve, ℓ_{total}^{shaft} = 19.3 mm on the shaft and the total length is 13.9 + 19.3 = 33.2 mm. As shown in Figs. 10c and 10d, the slip defect ④ has ℓ_{total}^{sleeve} = 14.3 mm on the sleeve, ℓ_{total}^{shaft} = 18.4 mm on the shaft and the total length is 14.3 + 18.4 = 32.7 mm. Table 7 summarizes those values. In Table 7, the total length for the defect ② and ④ are almost the same as the relative slip length of ℓ_s = 32.3 mm that is obtained from the slip specimen in Fig. 2. That being the case, it can be concluded that the starting point, as well as the ending point of the defects, can be evaluated accurately reflecting the real slip.

Table 7
Slip defect length ℓ_{total}^{sleeve}, ℓ_{total}^{shaft} in Fig. 8 observed on roll B in comparison with the slip distance $\ell_s = \pi d\theta_{slip}/360 = 32.3$ mm in miniature roll specimen in Fig. 2.

	ℓ_{total}^{sleeve}: Slip defect length on the sleeve (mm)	ℓ_{total}^{shaft}: Slip defect length on the shaft (mm)	$\ell_{total}^{sleeve}+\ell_{total}^{shaft}$: Total length (mm)
Slip defect ②	13.9	19.3	33.2
Slip defect ④	14.3	18.4	32.7

5. Fatigue strength evaluation of the real roll considering the slip and the defect

5.1. Three-dimensional defect geometry in miniature roll specimen

In this section, the geometry of the slip defect ② is identified. Then, the stress concentration factor of the ellipsoidal part is estimated, and finally, fatigue strength of the real roll is investigated considering the slip as well as the slip defect. For roll B, the geometry of the slip defect ② on the sleeve surface is identified by cutting the sleeve. Fig. 11 illustrates (a) the sleeve before cutting, (b) the sleeve after cutting, and (c) the enlarged view of the defect ② on the sleeve before cutting. A detailed identification of the defect depth geometry is carried out by observing the cross sections of AO and OB'.

Fig. 12 shows the AO cross section in Fig. 11. On the other hand, Fig. 13 shows the OB' cross section in Fig. 11. Figs. 12 and 13 portray the depth of 0.25 mm on AO cross section side and the depth of 0.17 mm on OB' cross section. Fig. 14 illustrates a three-dimensional shape of the defect. This elliptical part can be approximately assessed as $(x/a)^2 + (y/b)^2 + (z/c)^2 = 1$, (a= 1, b= 0.25, c= 4.0). Henceforth, the stress concentration factor of $K_t \cong 1.14$ can be estimated [40].

5.2. Stress amplitude and mean stress in real roll

In the previous paper as well as in Section 3, the interfacial slip was realized in the numerical simulation by applying the load shifting on the fixed roll surface to express the roll rotation [20–23]. In this section, the simulation can be applied to the real roll to evaluate the interfacial stress. Fig. 15 shows the dimensions of the real roll where fatigue strength should be evaluated. A standard load of $P = P_0 = 13270$ N/mm was applied to the real rolls that was used in the hot rolling [14,15]. In this section, fatigue strength is evaluated under a severe load of $P = 1.5P_0$, which considers the impact force during the plate biting as well as load variations due to the roll temperature change and setting error. Here, it is assumed that the shrink-fitting ratio is $\delta/d = 0.5 \times 10^{-3}$ and the friction coefficient between the sleeve and the shaft is $\mu = 0.3$ (see Appendix B) [20–23].

Fig. 16 shows an interface stress variation in the θ-direction due to two rotations of the loadshifting on a fixed roll. It is confirmed that one rotation and two rotations create almost the same stress variation in the θ-direction. Therefore, this section highlights the use of the stress obtained after two rotations to evaluate fatigue strength because of the high stability of the variation. In Fig. 16, the interface stress variation $\sigma_\theta^{P(0)\sim P(4\pi)}(\theta)$ due to the two rotations of the standard load of $P = P_0$ shifting is compared with the $\sigma_\theta^{1.5P(0)\sim 1.5P(4\pi)}(\theta)$ due to the two rotations of the severe load of $P = 1.5P_0$ shifting. The stress $\sigma_\theta^{P(0)\sim P(4\pi)}(\theta)$ due to

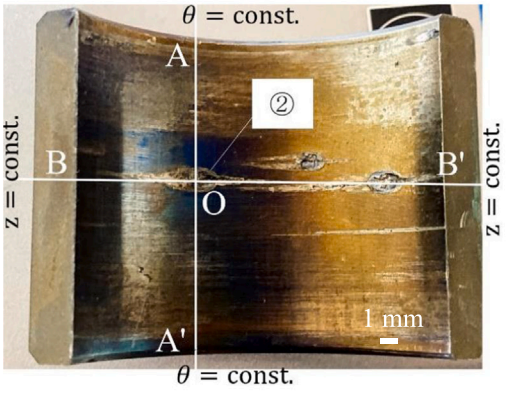

(a) Sleeve before cutting.

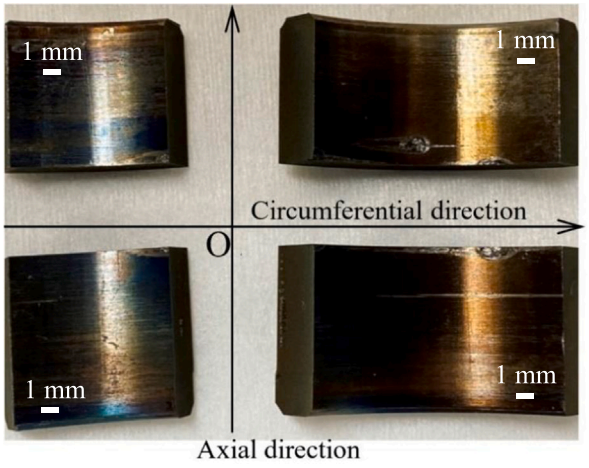

(b) Sleeve after cutting.

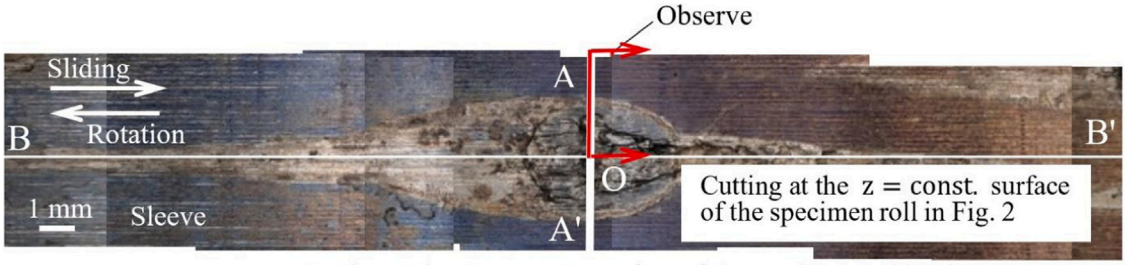

(c) Slip defect ② on the sleeve.

Fig. 11. Slip defect ② on the sleeve to identify defect dimension.

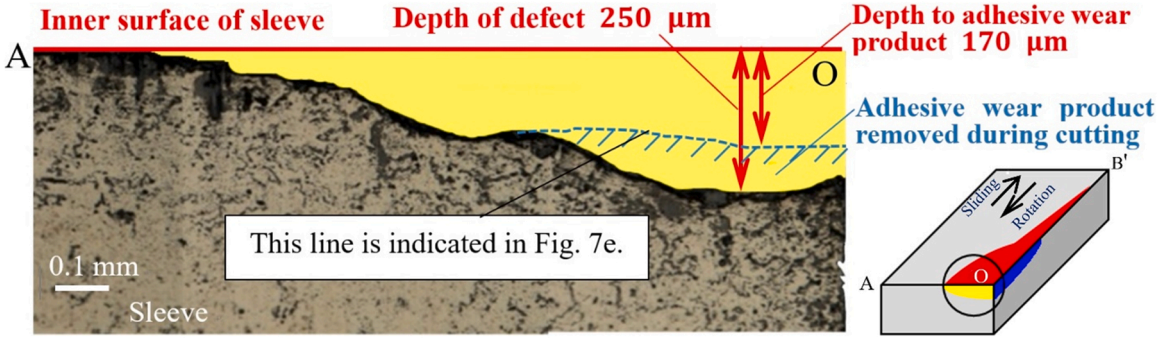

Fig. 12. Cross sectional observation of adhesive defect ② at the θ = const. surface of the sleeve in Fig. 11.

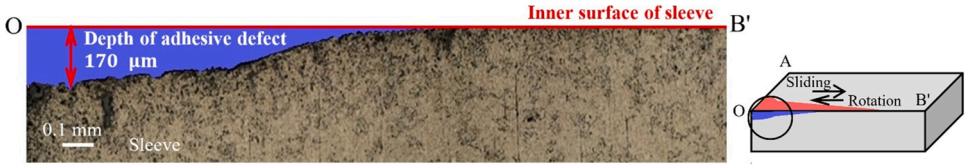

Fig. 13. Cross sectional observation of adhesive defect ② at the z = const. surface of the sleeve in Fig. 11.

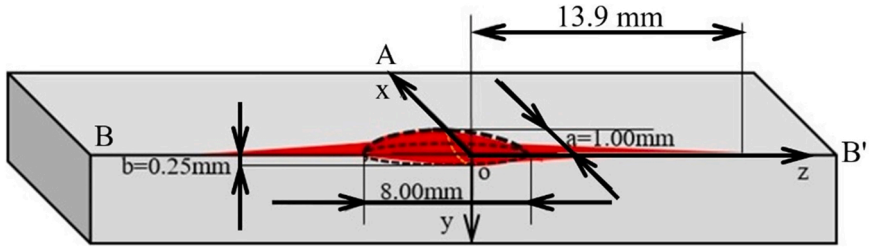

Fig. 14. Ellipsoidal plow defect ② geometry on the sleeve approximated by $(x/a)^2 + (y/b)^2 + (z/c)^2 = 1$, a = 1, b = 0.25, c = 4.0, $K_t \cong 1.14$.

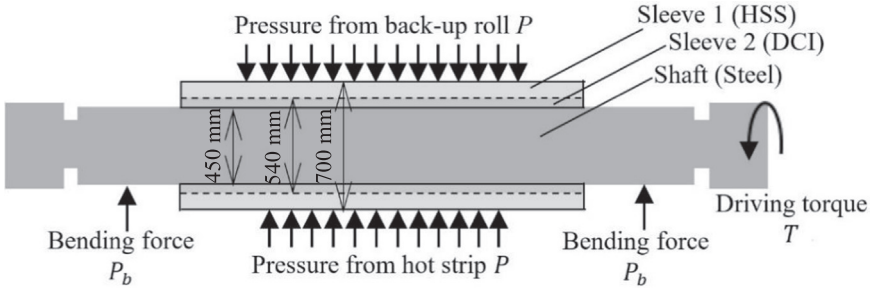

Fig. 15. Real sleeve roll geometry used in hot strip rolling to evaluate fatigue strength assuming the shrink-fitting ratio of $\delta/d = 0.5 \times 10^{-3}$ and the friction coefficient of $\mu = 0.3$ between the sleeve and the shaft.

$P = P_0$ has maximum stress of $\sigma_{\theta max} = 79.4$ MPa and the minimum stress of $\sigma_{\theta min} = 24.6$MPa. Instead, the stress $\sigma_\theta^{1.5P(0)\sim 1.5P(4\pi)}(\theta)$ due to $P = 1.5P_0$ has the maximum stress of $\sigma_{\theta max} = 91.3$ MPa and minimum stress of $\sigma_{\theta min} = -24.7$ MPa. Here, σ_a which denotes the stress amplitude and σ_m which denotes the average stress are expressed in Eqs. (4) and (5).

$$\sigma_a = (\sigma_{\theta max} - \sigma_{\theta min})/2 \tag{4}$$

$$\sigma_m = (\sigma_{\theta max} + \sigma_{\theta min})/2 \tag{5}$$

Under the standard loading of $P = P_0$, the stress amplitude of $\sigma_a = 27.4$ MPa and the average stress of $\sigma_m = 51.9$ MPa are obtained. Instead, under the severe loading of $P = 1.5P_0$, the stress amplitude of $\sigma_a = 58.1$ MPa and the average stress of $\sigma_m = 33.3$ MPa are obtained. With an increasing the load of 1.5 times larger, the stress amplitude σ_a increases by about 2.1 times larger and the average stress σ_m increases by about 0.6 times larger.

5.3. Fatigue strength evaluation of the real sleeve roll on the stress amplitude versus mean stress diagram

In this section, the fatigue strength of the real sleeve roll is evaluated by considering the circumferential slip. A similar defect identified in Section 5.1 that occurs in the real roll due to the slip is assumed. If the defect geometry is similar to the one observed in the miniature roll, the fatigue strength of the sleeve can be examined by using a stress concentration factor of $K_t \cong 1.14$ which was obtained for the slip defect ② in Fig. 14. Fig. 17 shows the stress amplitude versus the mean stress

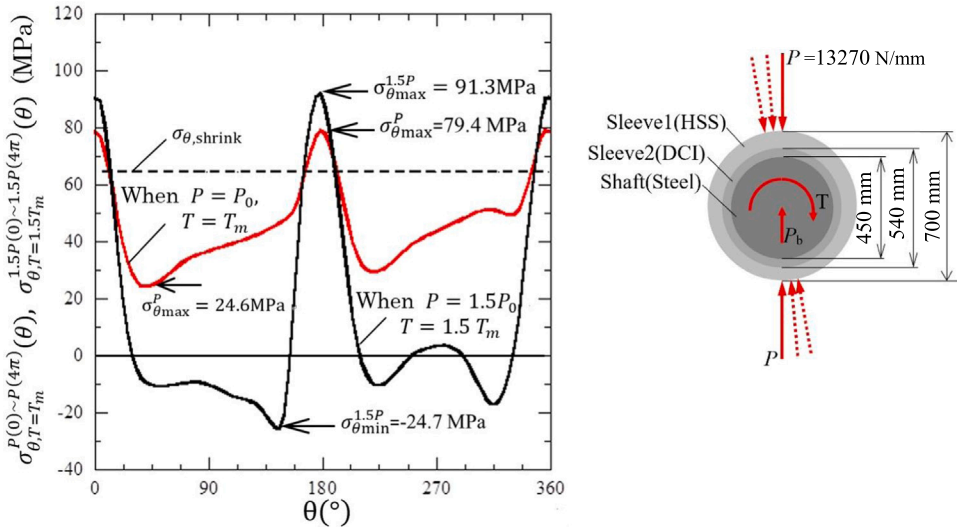

Fig. 16. Interface stress variation $\sigma^{P(0)\sim P(4\pi)}_{\theta,T=T_m}(\theta)$ due to the standard load of $P = P_0$ shifting in comparison with $\sigma^{1.5P(0)\sim 1.5P(4\pi)}_{\theta,T=1.5T_m}(\theta)$ due to the severe load of $P = 1.5P_0$ shifting in Fig. 15.

diagram (σ_a - σ_m diagram) for the stress σ_θ which appears at the inside of the sleeve. In this diagram, a tensile strength of $\sigma_B = 415$ MPa for the inner layer material DCI is applied and a fatigue limit of $\sigma_{w0} = 166$ MPa with the durability ratio of 0.4 is used. Point A in Fig. 17 shows the results $\sigma_a = 58.1$ MPa and $\sigma_m = 33.3$ MPa under a load of $P = 1.5P_0$, while considering the impact force explained in Section 5.2 as well as superposing the residual stress of 156 MPa as the mean stress. To evaluate the fatigue risk on the safe side, the stress concentration factor of $K_t \cong 1.14$ is multiplied by the results of Point A, thus, Point A' is shown. As shown in Fig. 17, even by using a severe loading of $P = 1.5P_0$, Point A is still located inside the endurance limit line. In addition, by considering the stress concentration of the defect, Point A' is also located inside the endurance line.

6. Conclusions

Shrink-fitted sleeve rolls have several advantages including the ability to reuse shafts by replacing worn sleeves, and the ability to apply to next-generation rolls. However, an interfacial slip may appear between the shaft and the shrink-fitting sleeve, which may damage the sleeve. In this paper, the interfacial slip was verified by using a miniature rolling mill experimentally with the aid of the numerical simulation studied recently. Then, the slip was confirmed under free rolling and the slip damage was identified. Considering the slip defects, fatigue strength was also discussed. The present approach and slip mechanism clarified in this paper can be applied to evaluating and improving the fatigue strength of the sleeve rolls and the next-generation rolls in further studies. The conclusions can be summarized as follows:

- Regarding the relative slip distance, the numerical simulation results are approximately 3.6 ~ 4.3 times larger than the experimental results for both shrink-fitting ratio of $\delta/d = 0$ and $\delta/d = 0.21 \times 10^{-3}$. This difference can be explained from a constant friction coefficient $\mu = 0.3$ assumed in the simulation, even though the friction coefficient is kept changing like $\mu = 0.3 \sim \infty$ throughout the experiment due to the growth of the slip defect. The comparison of the experimental results with the numerical simulation confirms the usefulness of the previous numerical simulation by Noda et al. [22,23].

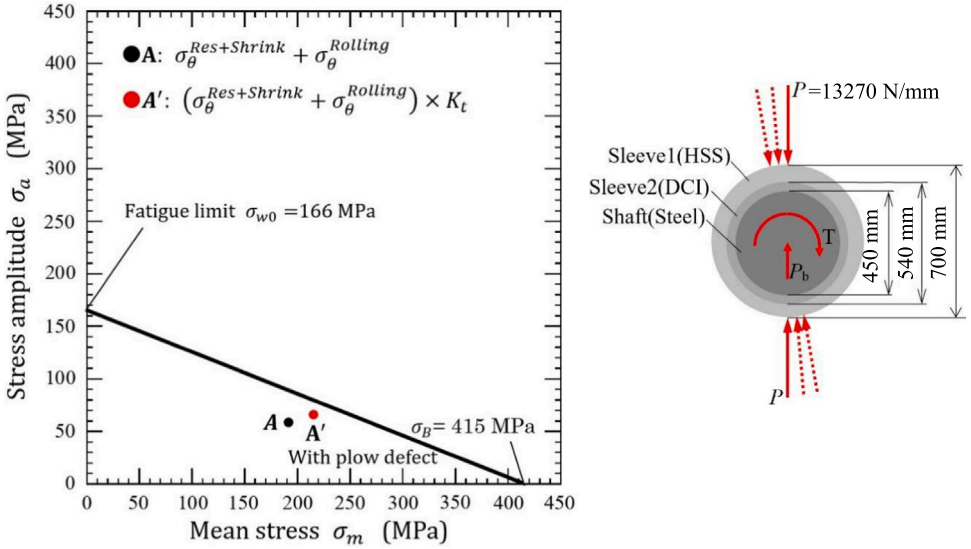

Fig. 17. Stress amplitude versus mean stress diagram ($\sigma_a - \sigma_m$ diagram) to evaluate the real sleeve roll fatigue strength based on the DCI tensile strength of σ_B = 415 MPa and DCI alternate fatigue strength of σ_{w0} = 166 MPa.

- The experiment and numerical simulation showed that under no shrink-fitting of $\delta/d = 0$, the slip distance becomes 2.79–3.53 times larger than the slip distance for $\delta/d = 0.21 \times 10^{-3}$.
- The slip defect can be formed in the following way. First, the slip defect starts with the contact of the surface roughness where the width is about to coincide with the pitch of the machining feed. Second, the slip defect is developed by the erosion and cohesive wear during the rolling. Finally, the slip defect forms a large oval-shaped erosion groove at the end of the scratch.
- The defects observed on the sleeve and the shaft can be classified into Region 1 ~ Region 5. The characteristics along with the changes of the regions are described, and the defect formation as well as growth were clarified.
- For the shrink-fitting ratio of $\delta/d = 0.21 \times 10^{-3}$ from the miniature roll experiment, the slip distance of $\pi d\theta_{slip} = 32.3$ mm which is obtained from the marked line coincides with the sum of defect that is observed on the sleeve and the shaft, for defect ②: 33.2 mm and for defect ④: 32.7 mm. This coincidence showed that the start and the end points of the defects were clearly identified.
- The three-dimensional defect geometry was identified. The total length of the slip defect is 13.9 mm, and the maximum depth is 0.25 mm. The stress concentration factor can be estimated as $K_t \cong 1.14$ by using the assumption of ellipsoidal shape approximation. The fatigue risk of the sleeve roll was estimated by using the dimensions and results obtained by numerical simulation while considering the slip.

Declaration of Competing Interest

The authors declare that they have no known competing financial interests or personal relationships that could have appeared to influence the work reported in this paper.

Acknowledgments

The authors would like to express our sincere gratitude to Hitachi Metals, Ltd., especially Dr. Nozomu ODA for their kind advice for the use of the hot rolling wear tester in Fig. 1 made by Hitachi Metals.

Funding

This research did not receive any specific grant from funding agencies in the public, commercial, or not-for-profit sectors.

Statement of Originality

The paper has not been published previously, that is not under consideration for publication elsewhere, and that if accepted it will not be published elsewhere in the same form, in English or in any other language, without the written consent of the publisher.

The paper does not contain material which has been published previously, by the current authors or by others, of which the source is not explicitly cited in the paper.

Appendix A. Supporting information

Supplementary data associated with this article can be found in the online version at doi:10.1016/j.triboint.2022.107793.

References

[1] Shimoda H, Onodera S, Hori K. Study on the residual deflection of large sleeved back-up rolls: 4th Report, Residual stresses of sleeved rolls. Trans Jpn Soc Mech Eng 1966;32:689–94. https://doi.org/10.1299/kikai1938.32.689.
[2] Takigawa H, Hashimoto K, Konno G, Uchida S. Development of forged high-speed-steel roll for shaped steel. Curr Adv Mater Process 2003;16:1150–3. https://cir.nii.ac.jp/crid/1573950399817369088.
[3] Irie T., Takaki K., Tsutsunaga I., Sano Y. Steel strip and section steel and thick rolling processing. Proc Iron Steel Inst Jpn, Tokyo 1979.
[4] Inoue T, Uchida S, Ogawa S. Characteristics of wear and rolling on fiber reinforced metal at high temperature. J Iron Steel Inst Jpn 2015;55:1987–93. https://doi.org/10.2355/isijinternational.ISIJINT-2015-123.
[5] Hattori T., Kamitani Y., Sugino K., Tomita H., Sano Y. Super cermet rolls for manufacturing ultra-fine-grained steel. Int Conf Tribol Manuf Process, Yokohama, 2007.
[6] Hamada S, Ogawa E, Shimizu K, Noda NA, Kishi K, Koga S. Development of large ceramic rolls for continuous hot-dip galvanized steel sheet production lines. Sokeizai 2010;51(12):54–9. ⟨http://hdl.handle.net/10228/00006066⟩.
[7] Mezentsev AV, Il'in VA, Syusyukin AY. Mastering of the technology of assembling of composite mill rolls under the conditions of rail and structural steel shop at the JSC "EVRAZ ZSMK". Metallurgist 2019;63(5):562–5. https://doi.org/10.1007/s11015-019-00860-5.
[8] Noda NA, Sano Y, Takase Y, Shimoda Y, Zhang G. Residual deflection mechanism for back-up roll consisting of shrink-fitted sleeve and arbor. J Jpn Soc Technol Plast 2017;58:66–71. https://doi.org/10.9773/sosei.58.66.
[9] Noda NA, Sakai H, Sano Y, Takase Y, Shimoda Y. Quasi-equilibrium stress zone with residual displacement causing permanent slippage in shrink-fitted sleeve rolls. Metals 2018;8(12):998. https://doi.org/10.3390/met8120998.
[10] Matsunaga E, Sano Y, Nishida S. Measurement of residual stress in high speed steel roll (Residual stress measuring of rolling roll by X-ray method-2). Curr Adv Mater Process 1997;10:1078.
[11] Matsunaga E, Tsuyuki T, Sano Y. Optimum shrink fitting ratio of sleeve roll (Strength design of shrink fitted sleeve roll for hot strip mill-1). Curr Adv Mater Process 1998;11:362. ⟨https://ci.nii.ac.jp/naid/10002551803⟩.
[12] Tutumi S, Hara S, Yoshi S. The residual deflection of sleeved back-up rolls. Tetsu-to-Hagane 1971;57(5):818–22. https://doi.org/10.2355/tetsutohagane1955.57.5_818.
[13] McMillan MD, Booker JD, Smith DJ, Onisa CF, Korsunsky AM, Song X, et al. Analysis of increasing torque with recurrent slip in interference-fits. Eng Fail Anal 2016;62:58–74. https://doi.org/10.1016/j.engfailanal.2015.12.005.
[14] Sano Y. Recent advances in rolling rolls. Proc of the No. 148-149 Nishiyama Memorial Technology Course. Tokyo 1993:193–226.
[15] Sano Y. Fatigue failure problem in the inside of roll body for hot strip rolling- Crack initiation problem and its estimation in the actual plant. The 245th JSMS Committee on Fatigue of Materials and The 36th JSMS Committee on Strength Design, Safety. Evaluation 1999:40.
[16] Matsunaga E, Tsuyuki T, Sano Y. Optimum shrink fitting ratio of sleeve roll (Strength design of shrink fitted sleeve roll for hot strip mill-1). Curr Adv Mater Process 1998;11:62. ⟨https://ci.nii.ac.jp/naid/10002551803⟩.
[17] Bataille C, Luc E, Bigerelle M, Deltombe R, Dubar M. Rolls wear characterization in hot rolling process. Tribol Int 2016;100:328–37. https://doi.org/10.1016/j.triboint.2016.03.012.
[18] Noda NA, Hu K, Sano Y, Ono K, Hosokawa Y. Residual stress simulation for hot strip bimetallic roll during quenching. Steel Res Int 2016;87(11):1478–88. https://doi.org/10.1002/srin.201500430.
[19] Hu K, Xia Y, Zhu F, Noda NA. Evaluation of thermal breakage in bimetallic work roll considering heat treated residual stress combined with thermal stress during hot rolling. Steel Res Int 2017;89(4):1700368. https://doi.org/10.1002/srin.201700368.
[20] Sakai H, Noda NA, Sano Y, Zhang G, Takase Y. Numerical simulation on interfacial creep generation for shrink-fitted bimetallic roll. J Iron Steel Inst Jpn 2019;59(5):889–94. https://doi.org/10.2355/isijinternational.ISIJINT-2018-749.
[21] Sakai H, Noda NA, Sano Y, Zhang G, Takase Y. Effect of driving torque on the interfacial creep for shrink-fitted bimetallic work roll. Tetsu-to-Hagane 2019;105(12):1126–34. https://doi.org/10.2355/tetsutohagane.TETSU-2019-048.
[22] Noda NA, Rafar RA, Sakai H, Zheng X, Tsurumaru H, Sano Y, Takase Y. Irreversible Interfacial Slip in Shrink-Fitted Bimetallic Work Roll Promoted by Roll Deformation. Eng Fail Anal 2021;126:105465. https://doi.org/10.1016/j.engfailanal.2021.105465.
[23] Rafar RA, Noda NA, Tsurumaru H, Sano Y, Takase Y. Novel design concept for shrink-fitted bimetallic sleeve roll in hot rolling mill. Int J Adv Manuf Technol 2022;120(3167–80):2. https://doi.org/10.1007/s00170-022-08954-.
[24] Noda NA, Rafar RA, Sano Y. Stress due to interfacial slip causing sleeve fracture in shrink-fitted work roll (pp) Int J Mod Phys B 2021:2140020. https://doi.org/10.1142/S0217979221400208.
[25] Soda N, Bearing Iwanami. Shoten, Tokyo 1964:196–203.
[26] Imai M. Creep of the roller bearing. Lubrication J Jpn Soc. Lubr Eng 1959;4(6):307–12.
[27] Murata J, Onizuka T. Generation mechanism of inner ring creep. Koyo Eng J 2005;166:41–7.
[28] Niwa T. A creep mechanism of rolling bearings. NTN Tech Rev 2013;81:100–3.
[29] Ten Sakajiri, Takemura Yukawa, Tech J NSK 2006;680:13.
[30] New Bearing Doctor: Diagnosis of bearing problems. Objective: Smooth & reliable operation. NSK, 1997. [accessed 28 June 2020]. https://www.nsk.com/common/data/ctrgPdf/e7005c.pdf.
[31] Zhan J, Takemura H, Yukawa K. A study on bearing creep mechanism with FEM simulation. Proc Int Mech Eng Congr Expo, Seattle 2007. https://doi.org/10.1115/IMECE2007-41366.
[32] Zhan J, Yukawa K, Takemura H. Analysis of bearing outer ring creep with FEM. Adv Tribol. Berlin 2009. https://doi.org/10.1007/978-3-642-03653-8_74.
[33] Noguchi S, Ichikawa K. A study about creep between inner ring of ball bearing and shaft. Proc Acad Lect Jpn Soc Precis Eng. Japan 2010. https://doi.org/10.11522/pscjspe.2010A.0.565.0.

[34] Teramoto T, Sato Y. Prediction method of outer ring creep phenomenon of ball bearing under bearing load. Trans Soc Automot Eng Jpn 2015;46:355–60. https://doi.org/10.11351/jsaeronbun.46.355.
[35] Bovet C, Zamponi L. An approach for predicting the internal behaviour of ball bearings under high moment load. Mech Mach Theory 2016;101:1–22. https://doi.org/10.1016/j.mechmachtheory.2016.03.002.
[36] Maiwald A, Leidich EFE. simulations of irreversible relative movements (creeping) in rolling bearing seats –Influential parameters and remedies. Proc World Congr Eng Comput Sci San Fr 2013;vol 2. ⟨http://www.iaeng.org/publication/WCECS2013/WCECS2013_pp1030-1035.pdf⟩.
[37] Schiemann T, Porsch S, Leidich E, Sauer B. Intermediate layer as measure against rolling bearing creep. Wind Energy 2018;21:426–40. https://doi.org/10.1002/we.2170.
[38] Sano Y.. PhD Thesis. Kyushu University, 1995.
[39] Hase A. Research cases and trends of wear mechanism. J Surf Finish Soc Jpn 2014;65:556–61. https://doi.org/10.4139/sfj.65.556.
[40] Murakami Y. The idea of stress concentration. Yokendo Publ Co Ltd Tokyo 2005:47.
[41] Sawamoto T. Precis Mach 1964;30:8.
[44] Marc Mentat team : Theory and User Information, Vol. A, MSC, Software, Tokyo, 2008; p. 713.